Strain and collapse during lithiation of layered transition metal oxides: a unified picture
SUPPLEMENTARY INFORMATION

Thibaut Jousseaume[1], Jean-Frans Colin[2], Marion Chandesris[3], Sandrine Lyonnard[4], and Samuel Tardif[5]

[1,4,5]Univ. Grenoble Alpes, CEA, IRIG, F-38000, Grenoble, France
[2,3]Univ. Grenoble Alpes, CEA, LITEN, F-38000, Grenoble, France

February 13, 2024

Contents

1 Particle diameter distribution

Measurements of particle diameter distribution is performed to confirm that the materials used have a similar particle design. After being scattered in an ultrasonic bath to avoid agglomerates, the three materials have a similar distribution with a mean diameter slightly decreasing with nickel enrichment. Note that for the three materials, around 7% (10% for LNO) have a diameter below 1μm, which likely corresponds to single crystals free from agglomerates.

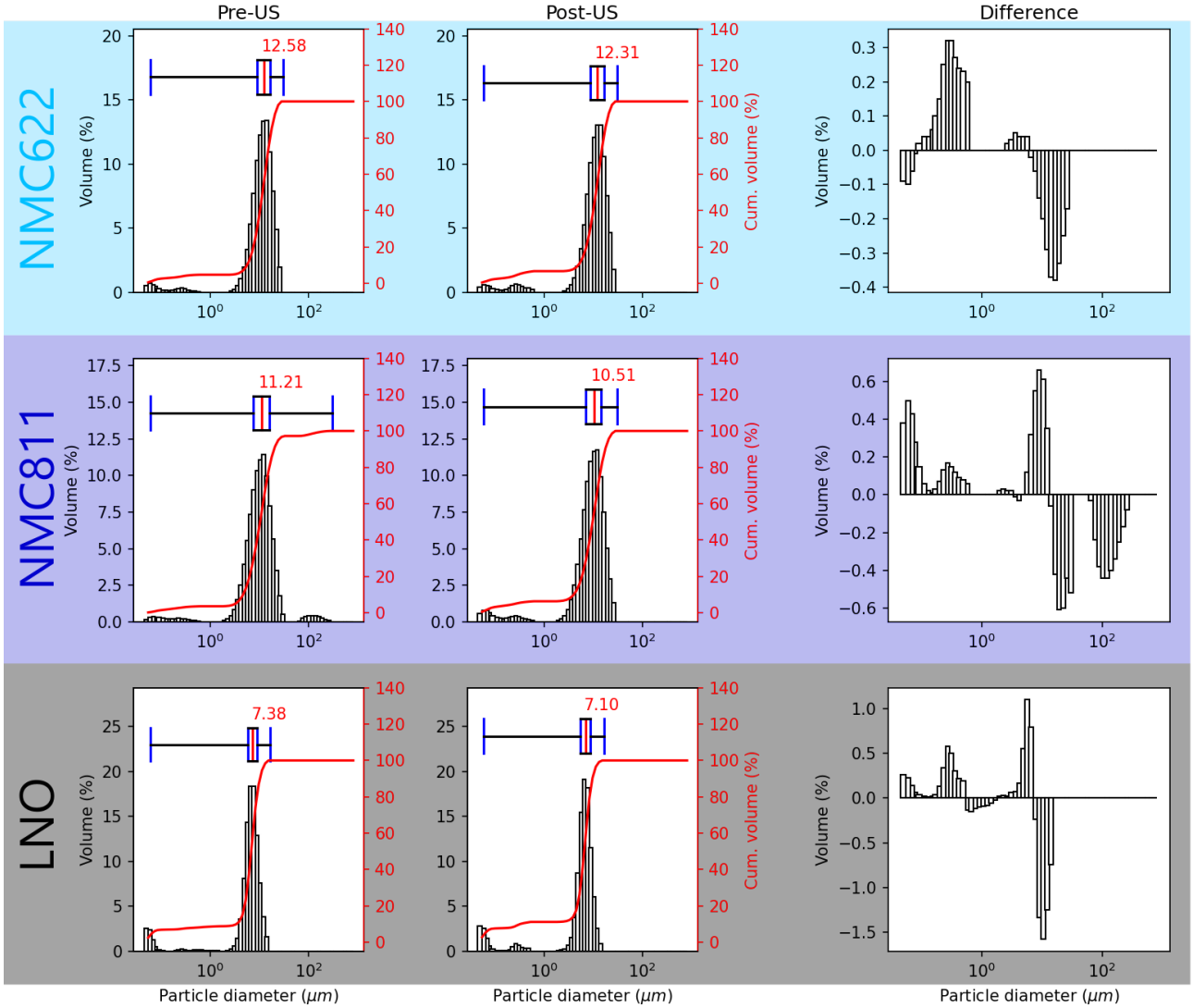

Figure S1: From left to right: Particle diameter distribution before ultrasonic bath, after ultrasonic bath, and the distribution of the difference. From top to bottom: NMC622, NMC811 and LNO particle distribution. The boxplot of the distributions are enclosed.

2 Pristine materials refinement

The pristine materials are refined with RIETVELD method to access atoms position. The refined parameters are shown in table S1. Additionally to the comments of the main text, one can note that nickel enrichement of neighbouring atoms makes the oxygen atoms less reduced, resulting in a weaker attraction to the nickel atoms. This is shown by the increase of the refined TM-O distance, $d_{\text{TM-O}}$. Then, despite being measured at same temperature, the thermal vibration of TM (Biso) decreases when the nickel content is higher whereas it should be the same. It is likely related to the TM delocalisation which assumes the three elements to have same characteristics in the layers (position, diameter). Yet Ni atom diameter being larger than Mn and Co atoms, it provides free moving space for the latter ones. The moving freedom and thermal vibration both result in the decrease of the Biso parameter with nickel enrichment.

	NMC622	**NMC811**	**LNO**
Space group	$R\bar{3}m$	$R\bar{3}m$	$R\bar{3}m$
a	2.8703	2.8727	2.8747
c	14.2255	14.2127	14.1775
z_O	-0.25807	-0.25840	-0.25821
Ni/Li exchange	2.16%	1.85%	2.78%
Biso of TM	0.23744	0.22043	0.15811

Table S1: Full refined parameters from RIETVELD unit cell refinement of pristine materials. "Ni/Li exchange" stands for the antisites rate of Ni/Li exchange, and "Biso" is the thermal vibration of TM atoms.

3 *Operando* XRD of NMCxyy charged at C/100

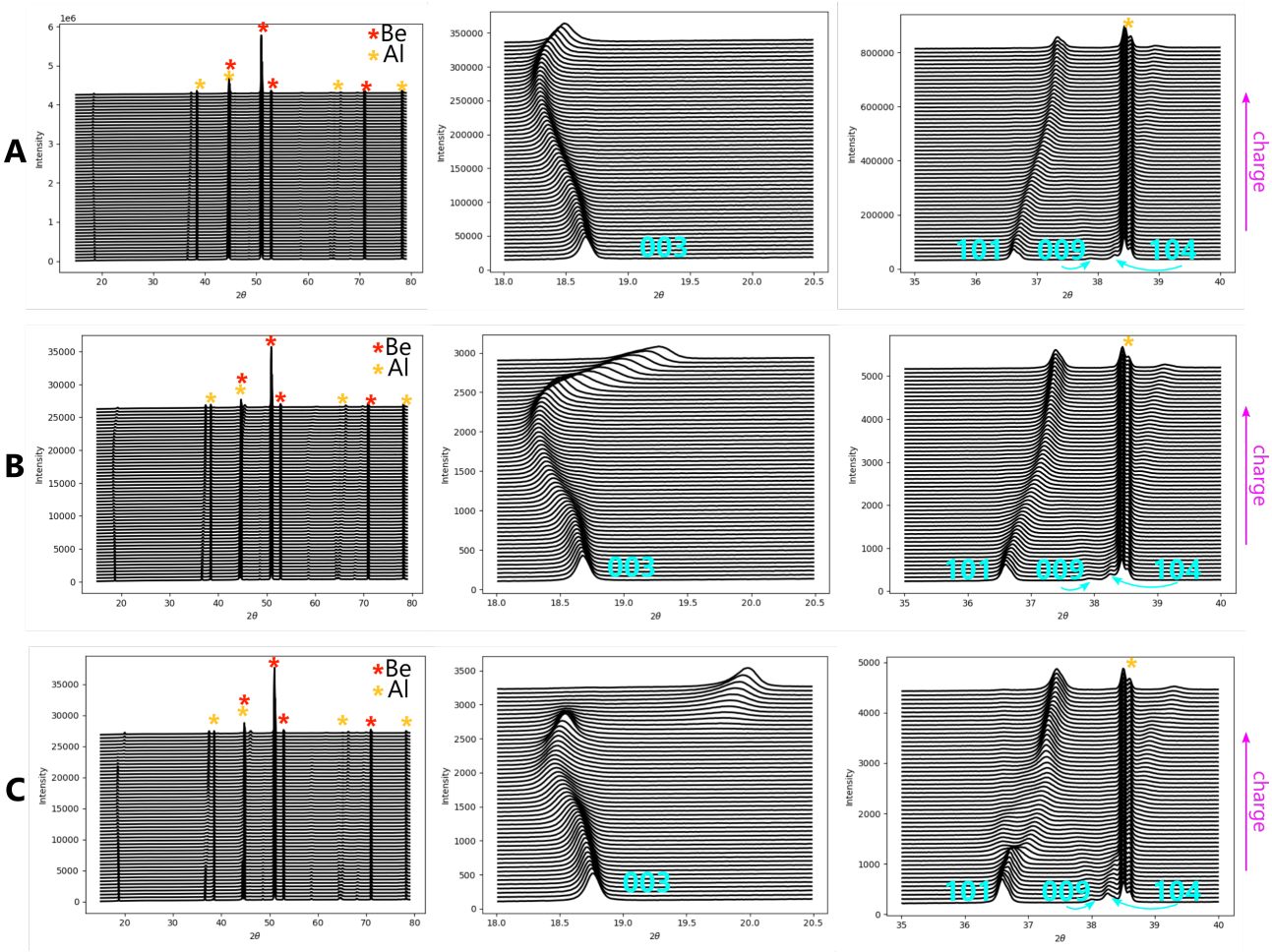

Figure S2: Full patterns and zooms in two intervals of *operando* measurement at C/100 with a lab diffractometer of (A) NMC622, (B) NMC811 and (C) LNO. The red and yellow stars label respectively the beryllium and aluminium diffraction peaks of the Leriche cell.

To test whether the multi-phases model or the single phase describe the best the data, the diffraction patterns were also fitted to the H1/H2/H3 phases model commonly used for the nickel-rich NMCs (Figure S3). The comparison of the results shows that the lattice parameters of the single phase model are sandwiched between the different phases of the H1/H2/H3 model. It suggests that the additional phases of the multi-phases model only fit the error caused by the shape of the peaks since the error is not significantly improved neither. This peak warping could be due to particles in late lithiation state due to a high resistance, as shown in Figure S4. Additionally, the multi-phases model does not best describe the end of the charge (worst error), when the H2→H3 is usually reported. The use of anisotropic strain instead seems to better suit the broadening of 00l reflections (Figure S3D).

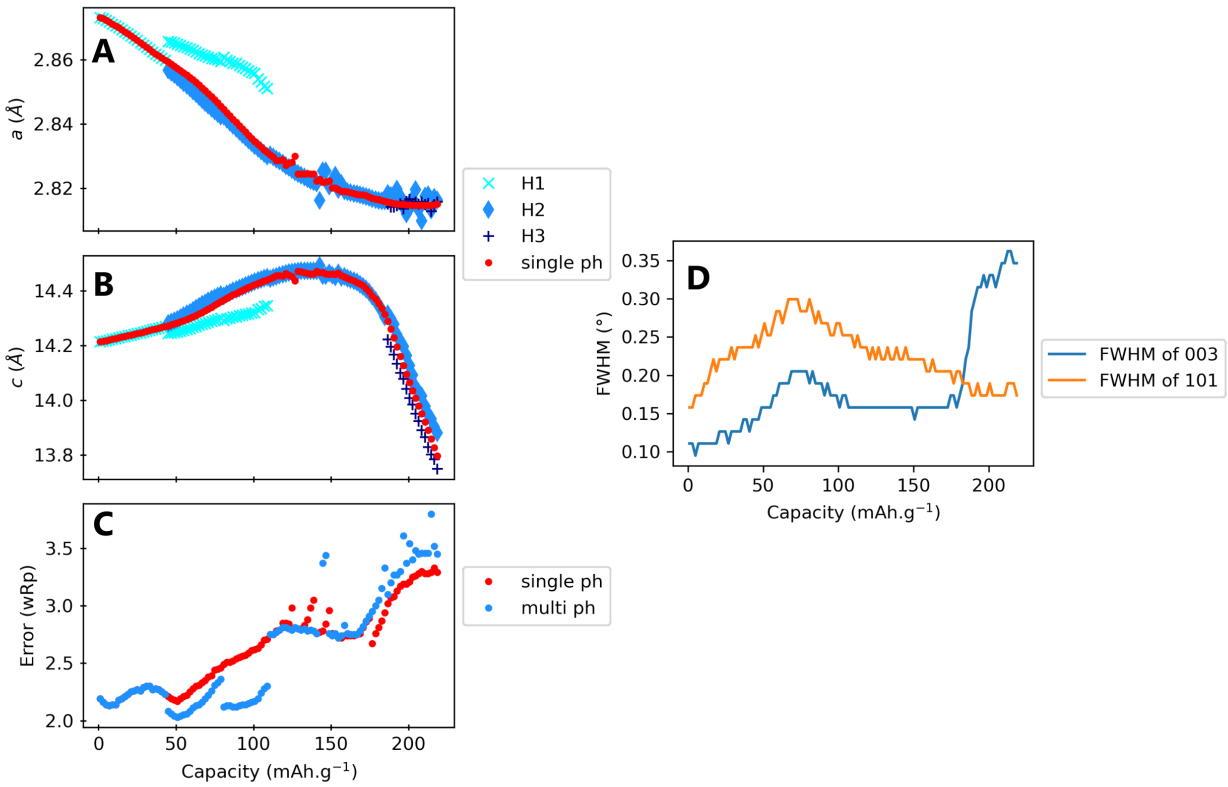

Figure S3: (A) and (B) Le Bail refinements of NMC811 lattice parameters charged at C/100 using two models: either a phase transition model in blue shades with the common H1, H2 and H3 phases (multi-phases model), or a single phase solid-solution model in red. (C) The refinement error. (D) FWHM of two selected NMC811 Bragg reflections.

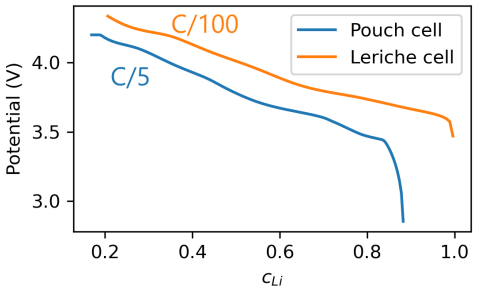

Figure S4: Potential curves of the two cells as a function of c_{Li}, *vs.* graphite at C/5 and *vs.* Li/Li$^+$ at C/100. The overpotential is higher in Leriche cell even though the C-rate is lower.

4 Calculation of the lithium content c_{Li}

The estimation of the lithium content in the materials is based on electrochemical data of the VSP potentiostat during the cycling. In particular, these data depicts the number of electrons exchanged with the electrodes. Set aside the few parasitic reactions occuring at the positive electrode, the electrons exclusively participate in the storage process of the lithium ions and of the SEI at the graphite electrode. As a consequence, the knowledge of the number of electrons exchanged is sufficient for a good estimation of the lithium content in the active material, the NMC.

The hypothesis of a very moderate electrode/electrolyte interface layer, that we assume, is valid since the coulombic efficiency of a NMC532 *vs.* Li/Li^+ is about 97% at the second conditioning cycle [1], which is quite good. In this study, they used the voltage range $[3.0, 4.5]$ V, which is known to be detrimental to the NMC, especially in the range $[4.2, 4.5]$ V. Furthermore the NMC electrode was cycled with a Li/Li^+ electrode, which is also detrimental to the electrode/electrolyte interface layer formation, as compared to a cycling with a graphite electrode [2]. Thus, in our case, the coulombic efficiency of the first cycles is expected to be significantly lower than 97%.

Additionally, assuming that there is indeed a quantity $c_{Li,\text{init}}$ of lithium used in the first cycles for the interphase layer formation at the positive electrode, $c_{Li,\text{init}}$ is expected to be the same for NMC622, NMC811 and LNO, since the presence of an atomic layer on the particles did not affect the coulombic efficiency in the first cycles [2]. Thus, it is possible that there is a systematic error in the c_{Li} estimation of the three materials, but if it exists, the error is expected to be limited to about 0.02.

The calculation of the lithium content c_{Li} in the NMCs is based on equation 1:

$$c_{Li} = 1 - \frac{C_m \cdot M_{\text{NMC}}}{\mathcal{F}} \cdot 3600 \tag{1}$$

with C_m the cumulative gravimetric capacity of the electrode ($\text{Ah}\cdot\text{g}^{-1}$), M_{NMC} the molar mass of the NMC used ($\text{g}\cdot\text{mol}^{-1}$), and $\mathcal{F}$ the Faraday constant ($\text{C}\cdot\text{mol}^{-1}$). C_m is obtained from the knowledge of the mass of the active material in each electrode used, and from the successive charge and discharge capacities measured by the potentiostat (Eq. 2):

$$C_m = \frac{\sum_i C_i}{m_{\text{AM}}} \tag{2}$$

with C_i the charge or discharge capacity (Ah), and m_{AM} the mass of active material in the electrode (g).

5 Charge rate impact on structure evolution of NMCs

Lattice parameters evolution of NMC622, NMC811 and LNO measured at C/100 by L-XRD is compared to refined parameters from pouch cells measured by S-XRD at higher C-rates (Figure S5). The materials investigated at C/100 were pristine, that is why their initial lithium content is higher, with higher a and lower c lattice parameters. The potential windows are different: every pouch cell are cycled between 2.5 V and 4.2 V *vs.* graphite. However, the LERICHE cells cycled from OCV reached 4.31 V, 4.34 V and 4.39 V *vs.* Li/Li$^+$ for NMC622, NMC811 and LNO, respectively (higher voltages could not be reached due to electrochemical instabilities). The differences potential windows is the origin of the small differences in the final state reached by materials cycled either in pouch or LERICHE cells.

The amplitude of lattice parameters variation is similar to higher C-rates for each material. Additionally, there is no change in space groups used to fit the patterns showing that the delithiation mechanism is the same. Yet, a shift in the lithium content estimated is suspected to be the cause of the differences at low and high kinetics. Since the Cu-Kα attenuation length is a few tens of microns, the particles probed are close to the current collector. Those particles are at a ahead charge state because the electrode is resistive as the potential curves show it, and it leads to the measured lithium content shift. This shift is hardly properly corrected, hence plotted as measured.

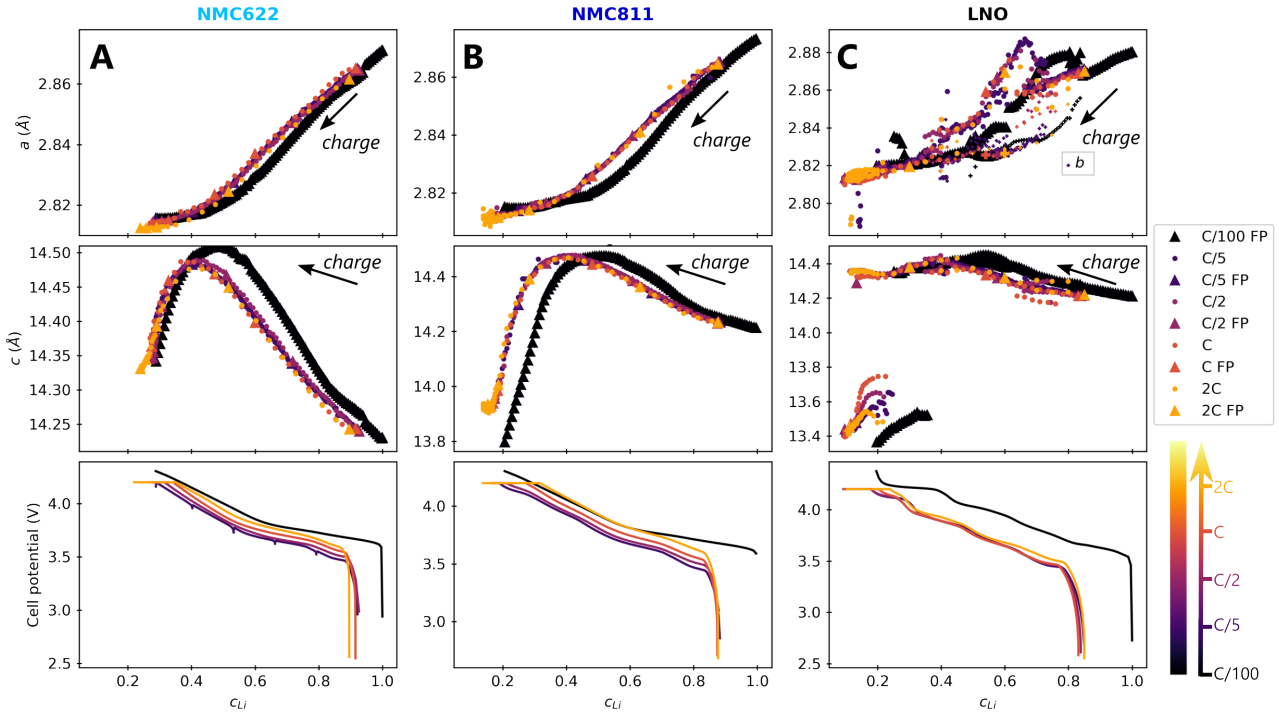

Figure S5: Structural evolution and potential curves of (A) NMC622, (B) NMC811 and (C) LNO as a function of lithium content c_{Li} for increasing charge rates from darker to lighter colors. The C/100 structure refinement are compared to S-XRD refinements (Figure 4). The C/100 data are measured in half cell configuration (*vs.* Li/Li$^+$).

6 Full dataset of refined NMCs parameters at different C-rates

Figure S6 is the entire dataset of refined parameters from the Le Bail method using the "fast refinement" procedure (see section 7). It includes parameters of H3 phase of LNO during the H2-H3 phase transition and that we are not confident with (see section 7). During the phase transition indeed, the XRD peaks belonging to H3 are highly broadened, which makes the fitting with only two phases without anisotropic strain less reliable. As a consequence, one can observe larger variation in lattice parameters during the 1st order phase transitions, especially seen at low Li content in the c lattice parameter (Figure S6C). This is due to the combination of local heterogeneity and phase transition in LNO. Both increase the XRD peak width, which finally broaden the fit results because we restrain the fit to a minimum of parameters: only two phases whose lattice parameters and isotropic strain are refined. The broadening of the results is supported by the fact that the lattice parameters evolution of LNO is not affected by the charge rate out of the phase transition domains. Note that the accuracy of the parameters obtained is ensured by the fit quality with anisotropic strain in the monophasic and biphasic (for LNO) domains (see section 7).

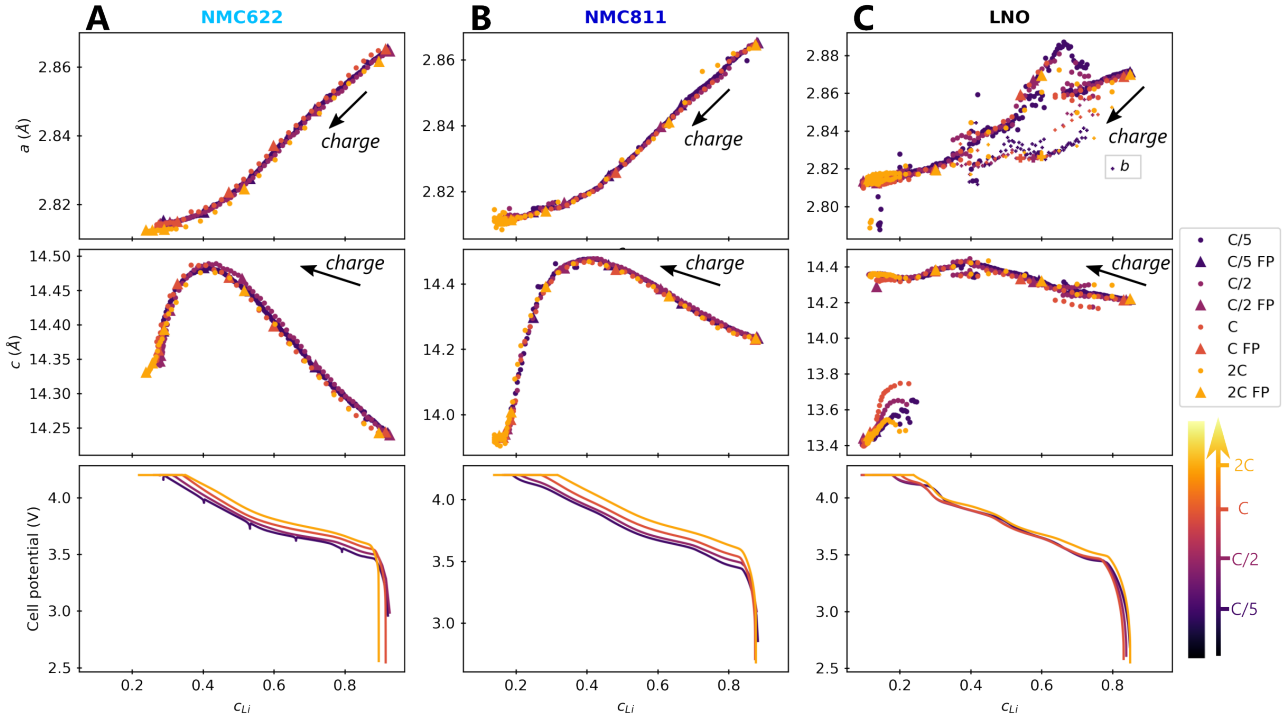

Figure S6: Data of Figure 4 completed with additional data of parameters obtained during the H2-H3 phase transition of LNO.

7 Fit quality during H2-H3 phase transition of LNO

This section shows why the refined parameters are less reliable in the biphasic domain of LNO, H2-H3, when we used the "fast refinement" procedure. This procedure limits the number of refined parameters (lattice parameters, isotropic strain) to provide stable fits in series. The fast refinement procedure is accurate in general, as depicted by the parameters obtained from the full pattern refinement with anisotropic strain that fall on the same curve (see Figure 4, 'FP' data points). It means that the averaged peak positions fitted by the fast refinement method accurately give the lattice parameters (Figure S7 A-C). Yet during the H2-H3 phase transition, the *hkl* peaks with high l components compared to h or k are highly broadened, making the averaged peak positions fitting less accurate (Figure S7 D-F). This results in a less stable parameters during the H2-H3 phase transition. This issue is settled when we used the full pattern refinement procedure with anisotropic strain (Figure S7 G-I). The latter procedure cannot be used while fitting patterns in series due to divergence issues.

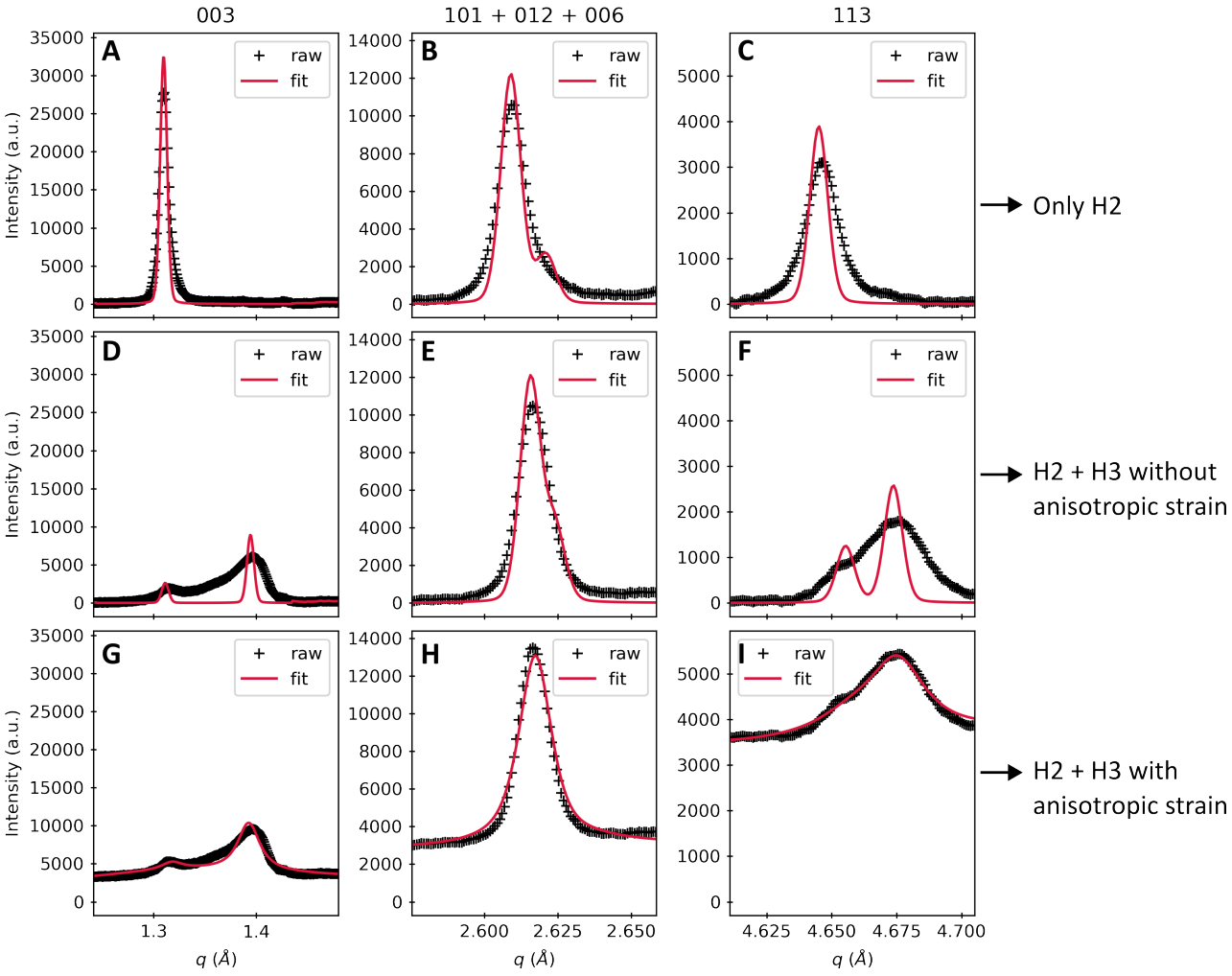

Figure S7: (A,B,C) Example of a refined pattern in a monophasic domain with isotropic strain but without anisotropic strain (H2). (D,E,F) Example of a refined pattern in a biphasic domain with isotropic strain but without anisotropic strain. (G,H,I) Same pattern than the second line, but refined with the anisotropic strain parameter.

8 NMC structure during the constant current step

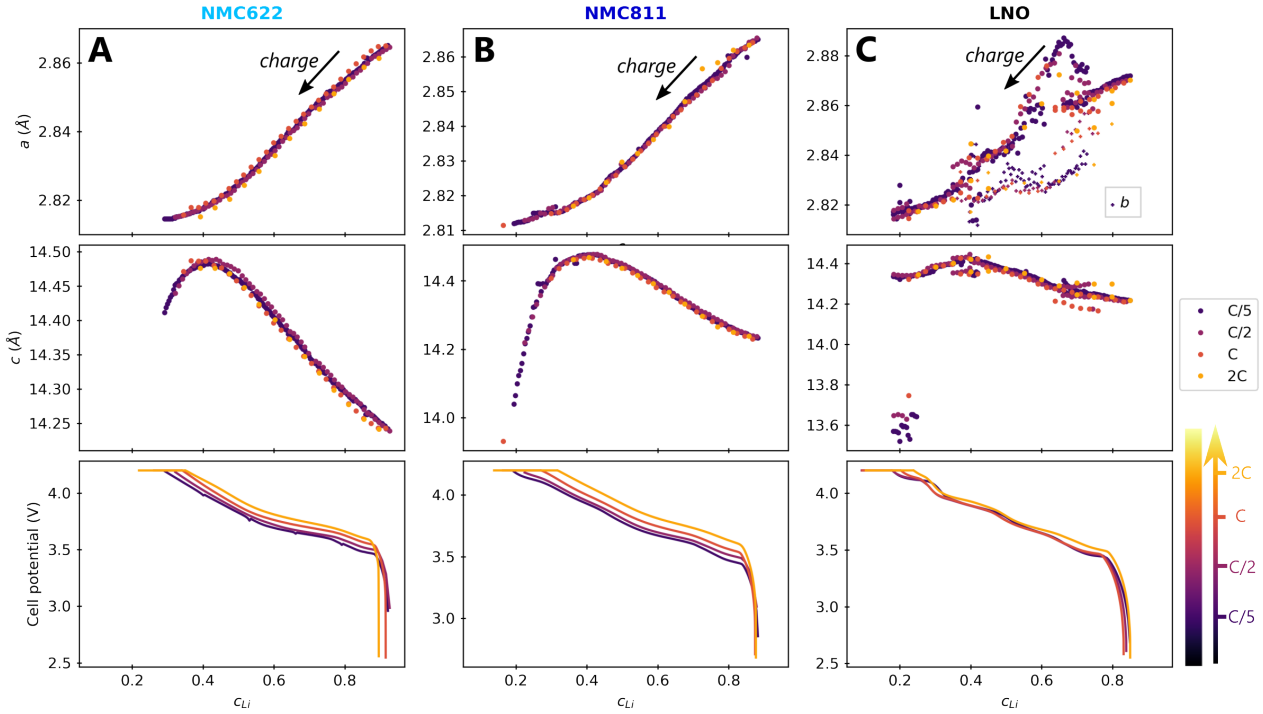

Figure S8: Structural evolution of various NMCs during the constant current step. Lattice parameters and potential curves of (A) NMC622, (B) NMC811 and (C) LNO as a function of lithium content c_{Li} for increasing charge rates from darker to lighter colors. The figure represents the same data than Figure 4, but without the constant voltage step.

9 NMC811 structure above 4.2V

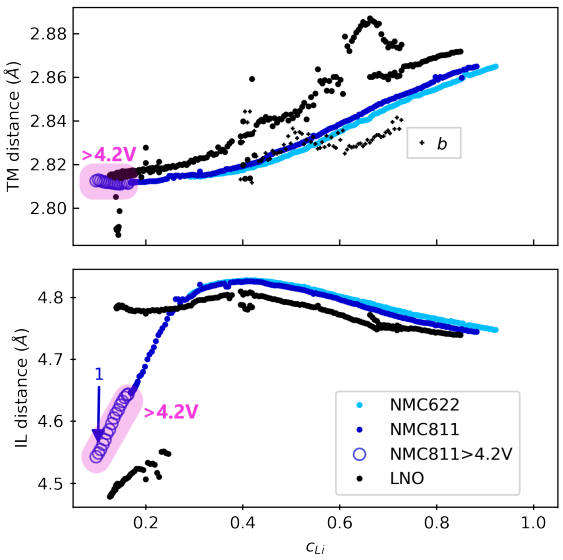

Figure S9: Structural evolution of NMC622, NMC811 and LNO as a function of lithium content c_{Li} at C/5. The curve with circle markers is NMC811 charged at C/5 between 4.2 V and 4.54 V (after a charge at C). The blue arrow points the measurement for which anisotropic strain is calculated (Figure 6B).

10 Comparison of lattice parameter evolution in a lab diffractometer

The comparison of lattice parameters evolution in Figure S10 A and B shows that NMC622, NMC811 and LNO evolve in concert, with similar lattice parameters values. The combined evolution is further confirmed with the derivatives of lattice parameters in Figure S10 C and D. The associated half cell potential is plotted in Figure S11.

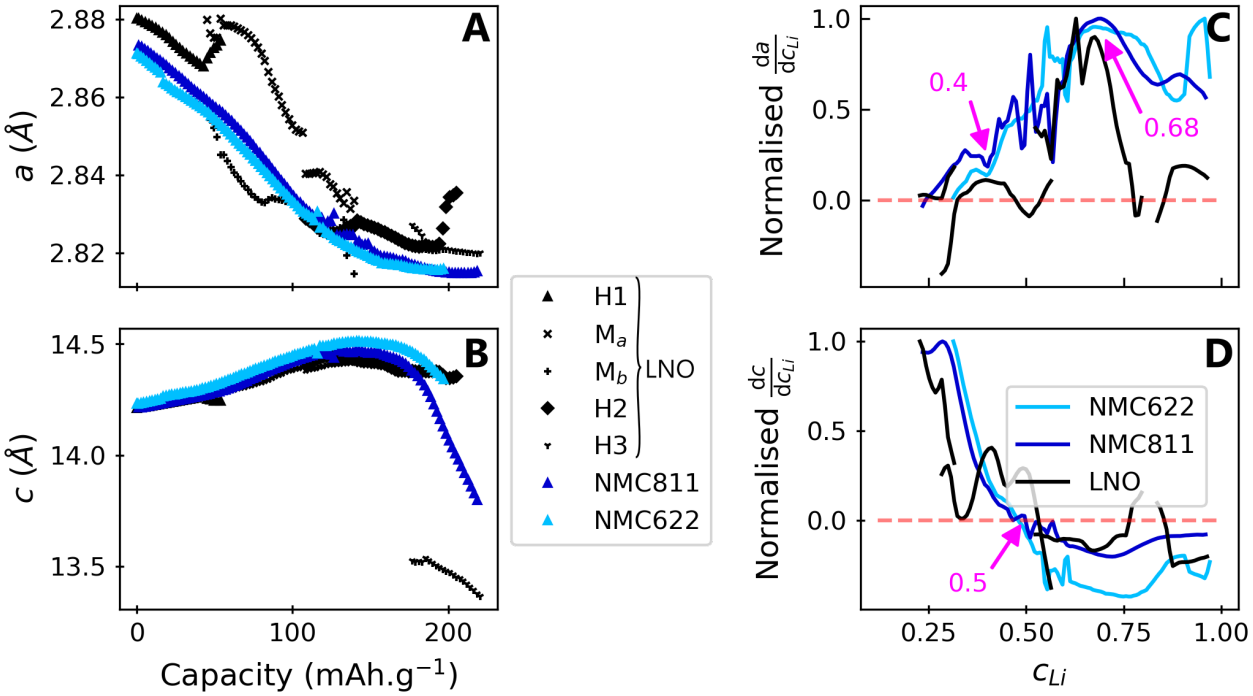

Figure S10: (A)(B) Evolution of refined lattice parameters of NMC622, NMC811 and LNO while charging at C/100.(C)(D) The associated derivatives of centered rolling mean lattice parameters by lithium content c_{Li}. The red dashed line stand for the zero. A non-linear shift in c_{Li} is known to exist and is plotted as measured since it cannot be suitably corrected. Nevertheless, it is a common shift to the three materials, justifying the comparison.

The lithium content c_{Li} of the materials is estimated from electrochemical files, but its absolute value may diverge from reality due to overpotential, and heterogeneities inside the cell used (Figures S4 and S5). It can also be due to the volume probed not representative of the bulk due to the absorption length of the beam (SI section 5). Despite a shift in the c_{Li}, the three specific c_{Li} discussed in the main text are highlighted at C/100 as well, but are shifted. The trend of lattice parameters derivatives appearing in Figure S10 is still relevant and with noteworthy key points: **(1)** NMC622 and NMC811 reaches the 0 value of $\frac{dc}{dc_{Li}}$ at a same $c_{Li} \simeq 0.5$, where c reaches its maximum. Here, the derivative of LNO is null between the M and H2 phase at $c_{Li} \approx 0.55$. **(2)** The plateau value of a is reached for the three materials at $c_{Li} = 0.4$, indicated by the common decrease of $\frac{da}{dc_{Li}}$. **(3)** The maximum value of $\frac{da}{dc_{Li}}$ is reached at a same $c_{Li} = 0.68$.

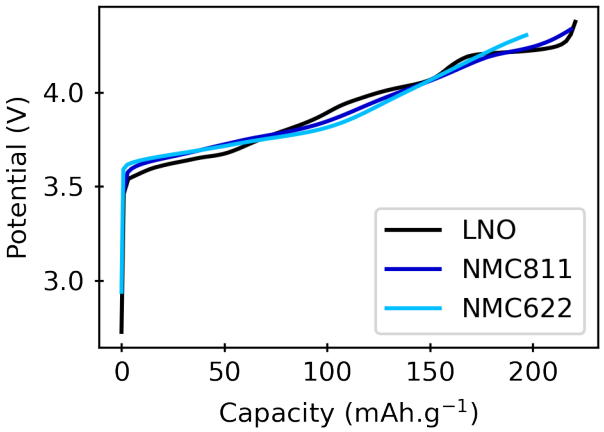

Figure S11: Potential of LERICHE cell of NMC622, NMC811 and LNO.

11 Mean lattice parameter c of LNO

In LNO, the inter-layer (IL) reaches its maximum during the phase transition M $\rightarrow$ H2, making more complex the definition of the maximum. We chose to interpolate the IL distance on single phased domains to make smoother the IL changes in that area. The polynomial curve of degree 12 is chosen to interpolate the data, and is shown in Figure S12A.

We varied the degree of the polynomial to ensure the stability of the root value. Changing the degree from 3 to 12 gives roots of $\frac{\mathrm{d}}{\mathrm{d}c_{Li}}(d_{\mathrm{IL}})$ in the interval $[0.382, 0.398]$. The curves of degree 11 and 12 significantly improved the fit (error 19.4% and 20.3% lower compared to degree 10, respectively), which is why the degree 12 is used. The root of the polynome of 12^{th} degree is $c_{Li} = 0.396$.

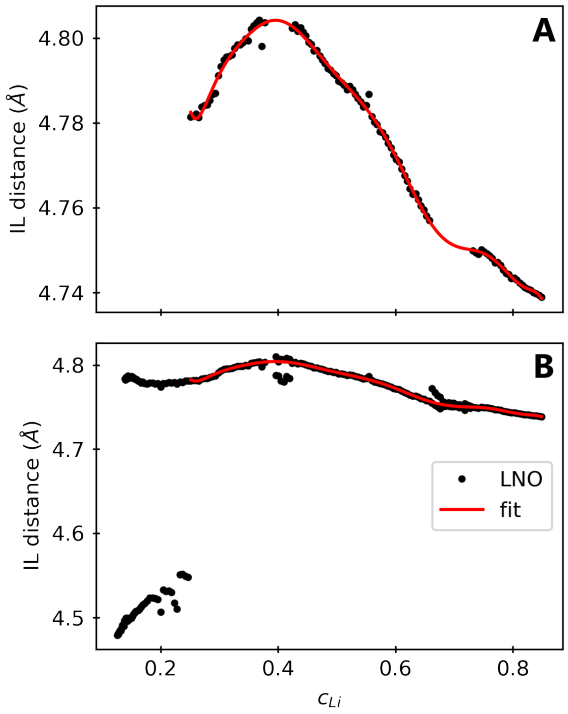

Figure S12: Refined IL distance of LNO as a function of lithium content c_{Li} at C/5 and its fit. (A) The fit is based on IL distance domains out of biphasic domains to get a smooth curve. (B) Overview of the interpolated curve in charge as calculated in (A) and compared to the full dataset of TM values, including biphasic domains.

12 Structural evolution upon discharge

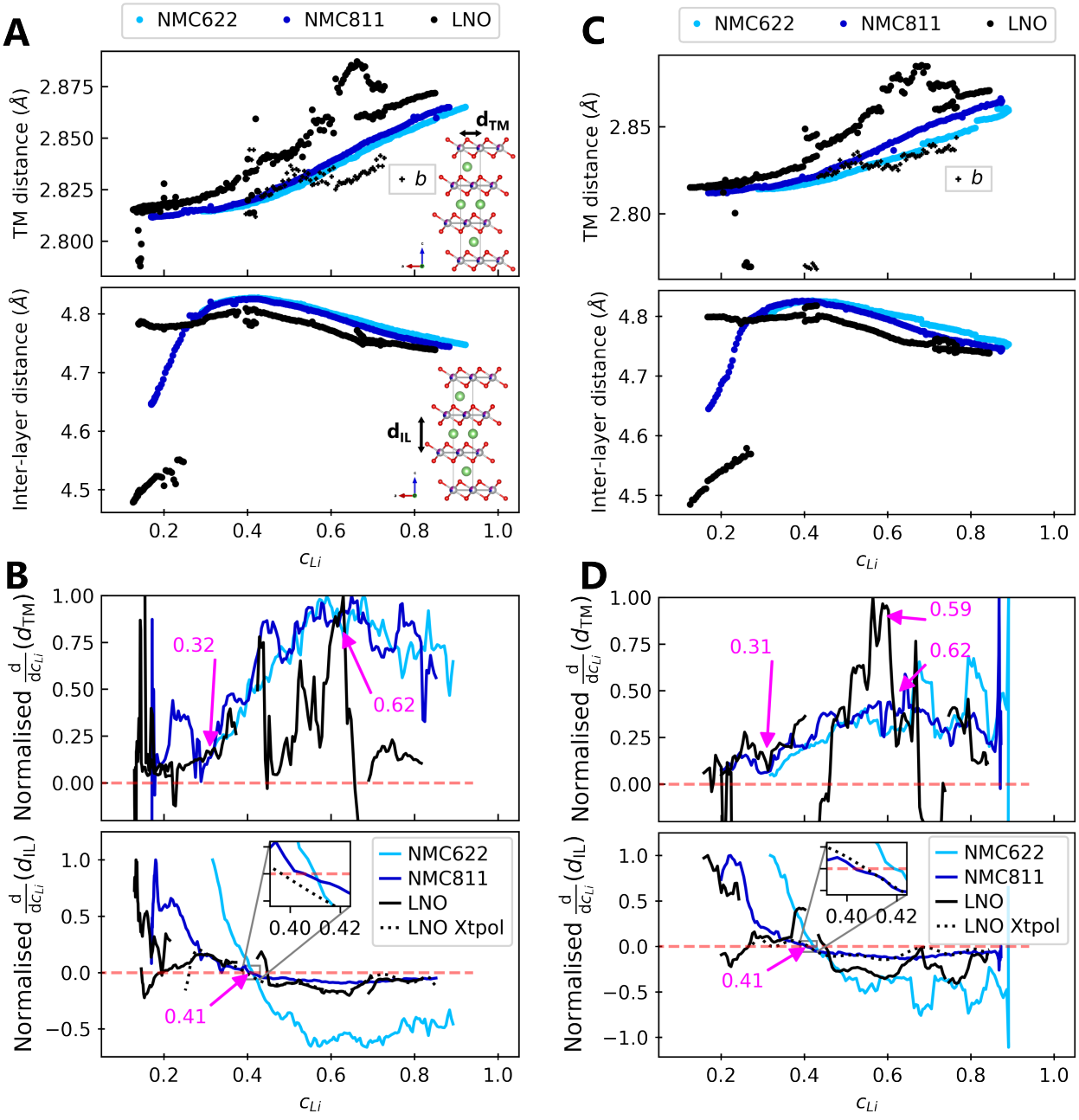

Figure S13: (A) TM distance and inter-layer distance (respectively a and $c/3$ for hexagonal symmetry) from refined lattice parameters of NMC622, NMC811 and LNO measured by S-XRD during a charge at C/5. (B) Derivatives of centered rolling mean lattice parameters by lithium content c_{Li} normalised by their respective maximum derivative value for NMC622, NMC811 and LNO, during a charge. The black dotted line is the derivative of the LNO extrapolation curve of c parameter defined in Figure S14. The red dashed line stand for the zero. (C) and (D) is the evolution during a discharge at D/5.

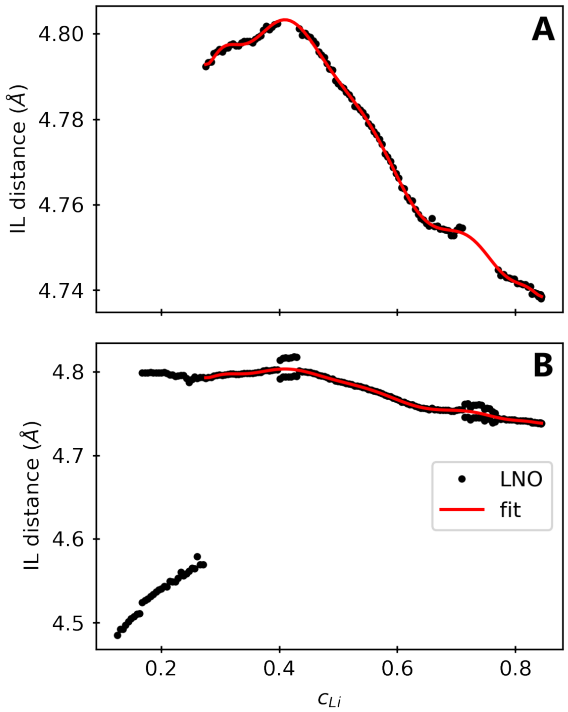

Figure S14: Refined IL distance of LNO as a function of lithium content c_{Li} at C/5 and its fit. (A) The fit is based on IL distance domains out of biphasic domains to get a smooth curve. (B) Overview of the interpolated curve in discharge as calculated in (A) and compared to the full dataset of TM values, including biphasic domains.

13 Comparaison of the strain impact and the SOC heterogeneity impact on Voigt curves

When using the traditional Voigt or pseudo-Voigt shape to fit XRD peaks, high care about the extracted parameters is called for. Indeed Pseudo-Voigt curve parameters are usually used to describe the strain with the gaussian parameter α and the crystalline domain size with the lorentzian parameter γ [3]. Those parameters suitably describe the sample characteristics when the experimental setup matches the theoretical model enough.

In the case of NMCs particles during charge, there is a common agreement in literature on lithiation heterogeneities between particles. This heterogeneity alters the shape of peaks, but do not significantly modifies the diffraction pattern since the heterogeneity of SOC is limited. Therefore, the sample cannot be considered as perfect because it is actually composed of a huge number of independent samples that look alike.

Here we show that the strain parameter of Voigt curve does not suitably describe the strain of the NMC materials. The effect of strain and of SOC heterogeneity are compared. The effect of strain is easily tunable by increasing the α parameter. The SOC heterogeneity is represented as a sum of Voigt curves of exact same gaussian and lorentzian parameters (α and γ), but with slightly different position. This sum of several Voigt curves is the peak shape expected if there were particles at different SOC with different lattice parameters, that is with different peak positions (Figure S15).

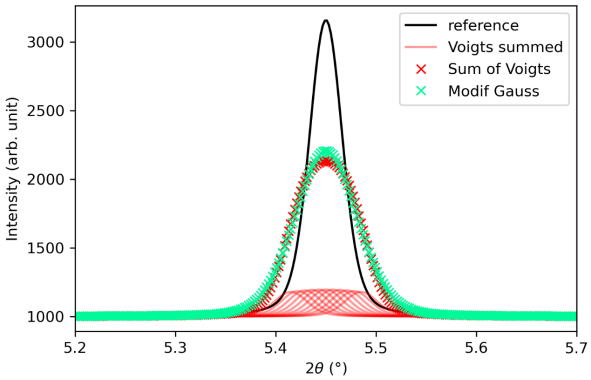

Figure S15: Definition of the two investigated curves, originating from the modification of a reference, a Voigt (plain black). The "Modif Gauss" is derived from the black curve but with a larger strain (α parameter). The "sum of Voigts" is also derived from the black curve, but with a sum of several Voigt curves, all parametrised with the exact same gaussian and lorentzian parameters (α and γ), and positioned at defined angles centered around the reference angle. The peaks have a decreasing amplitude, following a gaussian rule, that is function of their distance to the reference position.

The two modified curves are fitted and constrained by a γ fixed, assuming that the domain size does not change. Figure S16 shows that the fit with a modified Voigt is perfect. The zero error of the fit is related to the fact that the "Modif Gauss" is a still a Voigt curve, which has a gaussian parameter α modified compared to the reference curve. However, the "sum of Voigts" has of course non-zero residuals, because this peak shape cannot be perfectly fitted with a Voigt curve. Additionally, it can be noted that the shape of residuals are similar to the residuals of the 003 Bragg peak refinement that has been randomly selected. This shape of residuals can also be found in literature, for example the fit residuals of a real 111 ceria peak are very alike [3]. These results shows that it is not possible to distinguish a SOC heterogeneity from a broadening induced by strain using the common mathematical Voigt or Pseudo-Voigt curve in NMCs materials, and more generally in materials that are subject to solid-solution transformations. As a consequence, the strain obtained from the Le Bail or Rietveld refinement are biased, and does not accurately describe the actual strain endured by the NMCs.

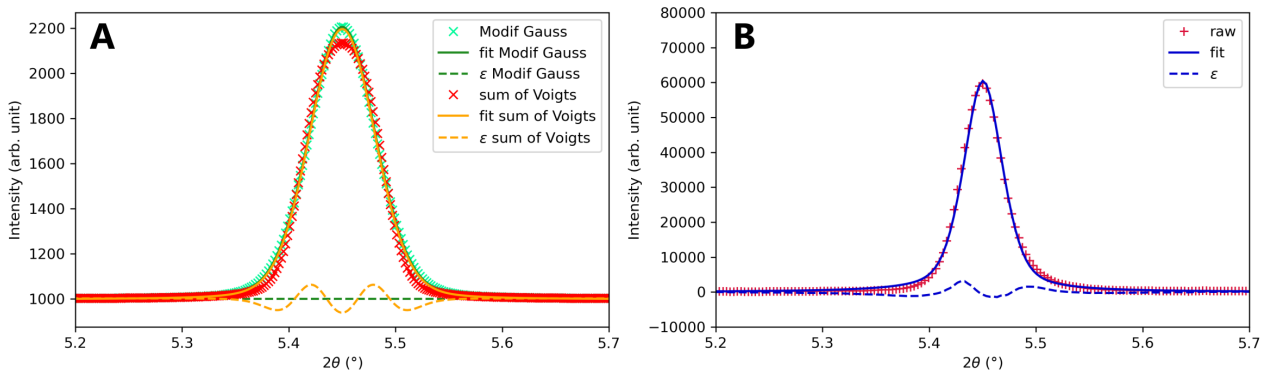

Figure S16: (A) In green shades, the Voigt curve with modified lorentzian parameter (0) (cross), its fit with a Voigt (plain) and its residuals (dashed). In red shades, the sum of Voigts curve (cross), its fit with a Voigt (plain) and its residuals (dashed). The residuals of the Voigt curve with $\gamma = 0$, that is a Lorentzian, are null. The residuals of the sum of Voigts are negatives on the peak borders and present two positive bumps near the peak center. (B) An example of a 003 NMC622 peak (cross), fitted with a pseudo-Voigt (plain), and its residuals (dashed). The residuals are also negatives on the peak borders, and are positives two times near the peak center.

14 Anisotropic strain evolution in a lab diffractometer

The anisotropic strain analysis is also performed on the data collected in the lab diffractometer at a slow charging rate. At C/100, the anisotropic strain is appearing at a same charging capacity for NMC622, NMC811 and LNO. Since the charging current is the same and assuming the same side reactions are taking place for the three materials, it shows that anisotropic strain is increasing at a same lithium content for the three materials. For LNO the anisotropic strain is bound to H3 phase only, it increases during the phase transition H2→H3 and begins to decrease when only H3 exists. C/100 charge rate cannot be directly compared to the other charge rates because of a lithium content shift hardly corrected, and related to the *in situ* cell as evidenced in Figure S5.

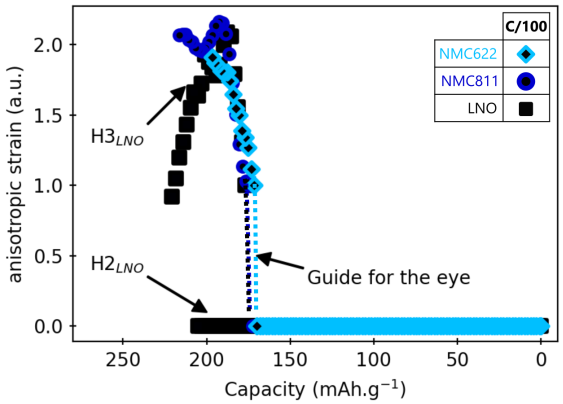

Figure S17: Anisotropic strain from Le Bail refinement of the full patterns as a function of capacity for each of the three materials investigated charged at C/100. Same shape of markers are used for all LNO phases for more clarity. The anisotropic strain is fitted when it does not tend to zero.

15 A reversible anisotropic strain evolution in discharge

The pouch cells charged at C/5 were also discharged at C/5, and C/2 for NMC622. Anisotropic strain analysis is then performed on randomly selected discharged diffractograms of NMC622, NMC811 and LNO. The anisotropic strain values falls again on the same exponentially increasing master curve that we evidenced in charge. The strain decreases to zero between $c_{Li} \simeq 0.4$ and $c_{Li} \simeq 0.5$.

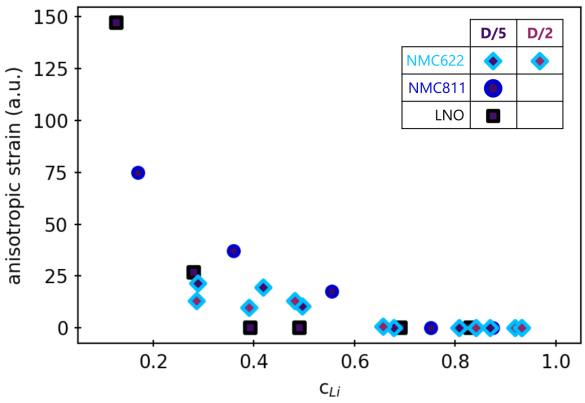

Figure S18: Anisotropic strain from Le Bail refinement of the full patterns as a function of the lithium content for each of the three materials investigated, when discharged at C/5 or C/2. Same shape of markers are used for all LNO phases for more clarity. The anisotropic strain is fitted when it does not tend to zero.

16 Effect of the local lithiation heterogeneities on the peak shape

Local heterogeneities of lithiation are associated with local heterogeneities of lattice parameters, which is assessed here based on simulated data. The broadening of lattice parameters values can be followed by estimating the widths ratio of Bragg peaks which have unbound $\langle hkl \rangle$ components. The 003/113 widths ratio is investigated because of its high sensitivity to the anisotropic effects, coming from the 003 reflection. The experimental or simulated width is evaluated from the integral breadth (IB) given in Eq. 3:

$$\mathrm{IB} = \Big(\int_{\theta} I d\theta \Big) / \max(I) \tag{3}$$

with I the intensity. The IB is convenient since it does not rely on any assumptions on the mathematical shape of the peak.

The simulated widths are calculated from simulated diffraction patterns, that take into consideration the heterogeneity of lattice parameters at a defined c_{Li}. Assuming a normal distribution of lithiation state at a defined $c_{Li,j}$, and knowing the lattice parameters evolution as function of c_{Li} (from Figure 7A and 7B of the main text), one can estimate the distribution of lattice parameters at this $c_{Li,j}$. The distributions of lattice parameters at selected $c_{Li,j}$ compositions are given in Figure S19.

The structure and multiplicity factors must be considered in the peak intensity calculations, so as the oxygen position. The peak intensity also depends on experimental factors such as the absorption factor or the Lorentz factor. All the factors aforementionned are considered in the calculation of the simulated diffraction patterns. The parameters are calculated for 8 c_{Li} compositions ranging from $c_{Li} = 0.22$ (delithiated) to $c_{Li} = 0.92$ (lithiated). The effect of temperature (no impact when considering the width ratio), polarisation (weak for synchrotron radiation), and of preferred orientation (weak for NMCs) are not evaluated.

Now that the ideal theoretical diffraction patterns without heterogeneities at $c_{Li,j}$ labelled $\mathcal{D}_p^{c_{Li,j}}$, and the associated lattice parameter distribution are known, it is possible to build the simulated diffraction patterns with local heterogeneities. Those assume that the structure factor at a defined $c_{Li,j}$ is constant within the vicinity of $c_{Li,j}$, that is, is constant within $[c_{Li,j} - \Delta c_{Li}/2, c_{Li,j} + \Delta c_{Li}/2]$. The diffraction patterns are calculated according to Eq. 4:

$$I_{\Delta c_{Li}}^{c_{Li,j}}(2\theta) = \int_{x_{Li}} f(x_{Li}) \cdot \mathcal{D}_p^{c_{Li,j}}(2\theta) \mathrm{d}x_{Li} \tag{4}$$

with $f \sim \mathcal{N}(c_{Li,j}, (\Delta c_{Li})^2)$.

It is now possible to calculate the ratio $\mathrm{IB}_{003}/\mathrm{IB}_{113}$ for various Δc_{Li} as a function of c_{Li}. The comparison of this ratio calculated from simulated patterns to the same ratio calculated from the experimental patterns is shown in Figure S20. The evolution of the experimental and simulated widths ratio is very similar. These results suggest that the local lithiation heterogeneities are weak at the beginning of the charge (highly lithiated) since the experimental widths ratio is almost constant. However, below $c_{Li} = 0.3$, the ratio severely increases, meaning that the local heterogeneity increases as well. The estimation of the local heterogeneity at $c_{Li} = 0.2$ from Figure S20 gives an approximate value of $\Delta c_{Li} = 0.25$ or $\Delta c_{Li} = 0.5$. The local heterogeneity estimation cannot be more precise with this analysis method since the ratio intensity decreases for very large Δc_{Li} values (> 0.3).

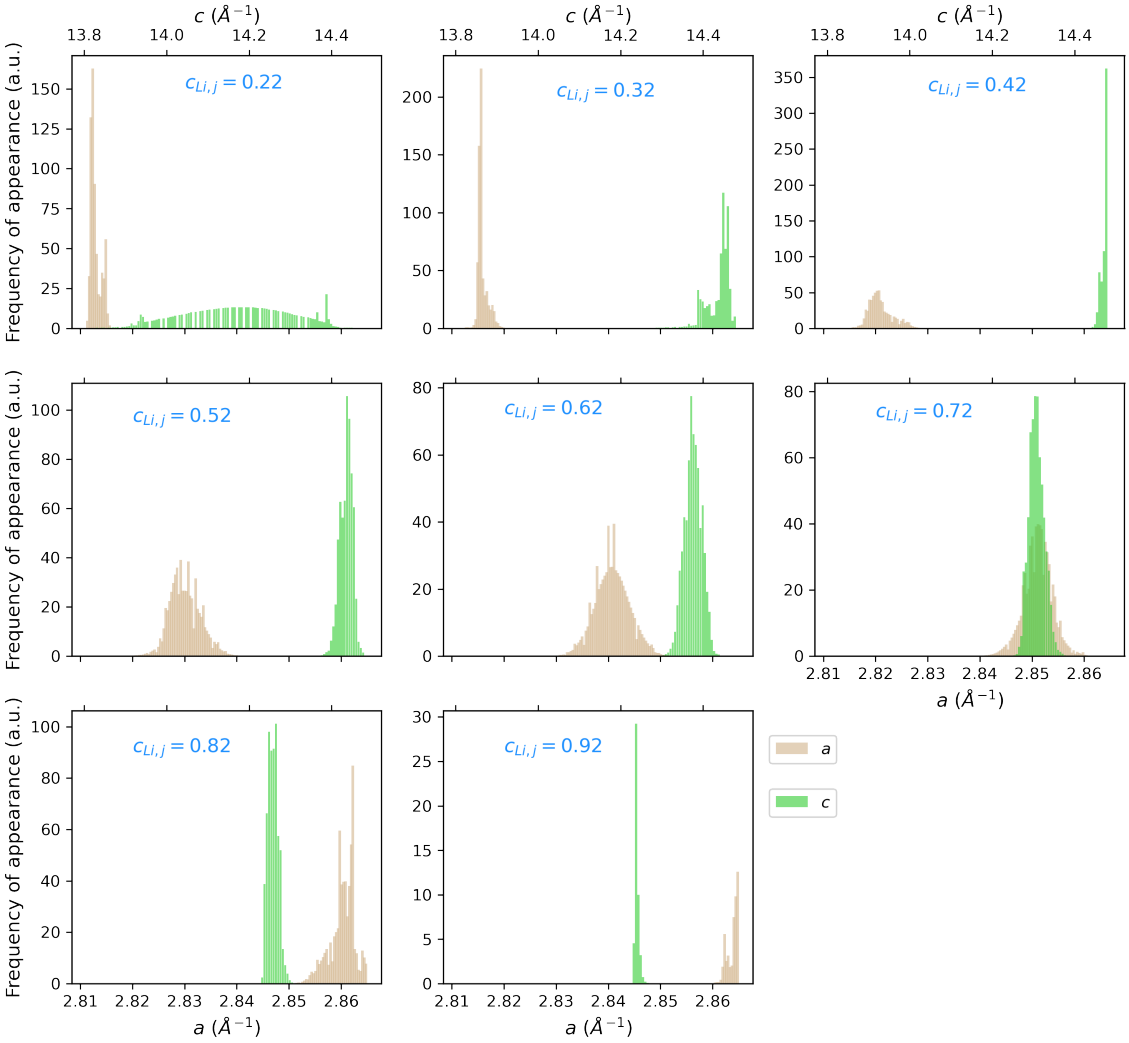

Figure S19: Lattice parameter distribution of NMC811 at different c_{Li} for a local heterogeneity $\Delta c_{Li} = 0.03$. The distribution is calculated at each c_{Li}, and estimated from a normal distribution of parameters $\mu = c_{Li}$ and $\sigma = \Delta c_{Li}$.

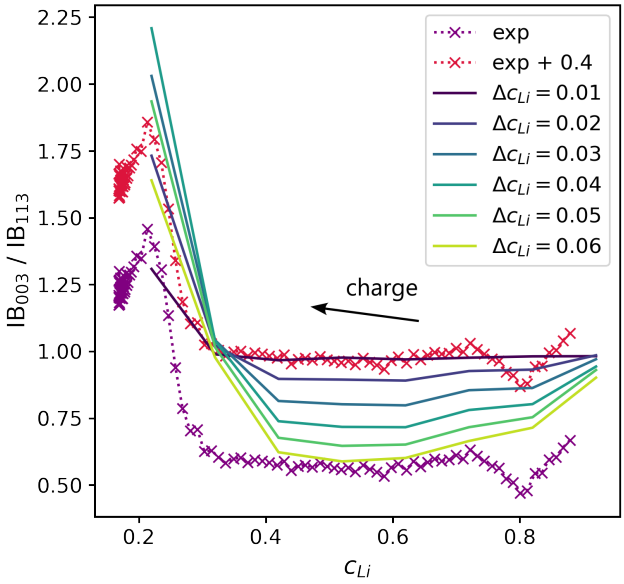

Figure S20: Comparison of the evolution of the relative integral breadth (IB) of the 003 *vs.* 113 Bragg peak as a function of c_{Li}. The purple cross stands for the raw ratio IB_{003}/IB_{113}, and the dark red cross stands for the raw ratio y-shifted of 0.4.

17 Peak widths for increasing charge rate

The inter-crystal strain is estimated here. To a first approximation, the inter-crystal strain is linked to the extent of heterogeneity in the depth of the particle. Thus, a larger heterogeneity induces a larger peak width. Yet in NMC622 and NMC811, the C-rate affects the peak width only at high c_{Li} (SI-17). This is likely due to the low solid lithium diffusion limiting the kinetic when the lithium layers are almost full [4, 5, 6, 7]. This is in agreement with Qian *et al.* results showing that inter-crystal strain is higher for faster charge rate [8]. The analysis technique used does not allow to conclude on LNO's case due to its phase transformations.

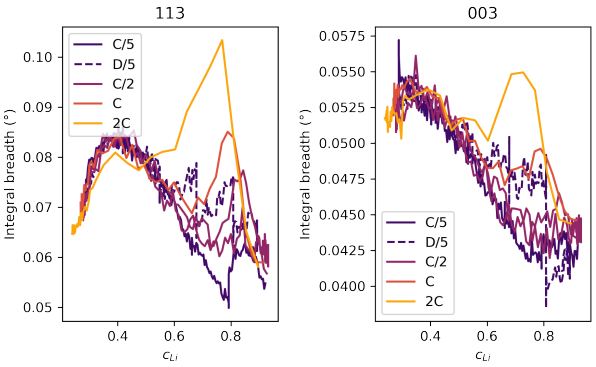

Figure S21: Integral breadth (IB) of 113 and 003 Bragg reflections of NMC622 as function of lithium content c_{Li} for increasing charge rates (C/5, C/2, C, 2C).

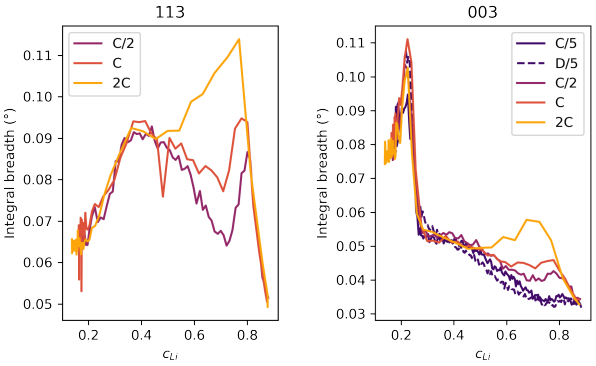

Figure S22: Integral breadth (IB) of 113 and 003 Bragg reflections of NMC811 as function of lithium content c_{Li} for increasing charge rates (C/5, C/2, C, 2C). The IB of 113 at C/5 is not calculated due to an anomalous peak in this q range.

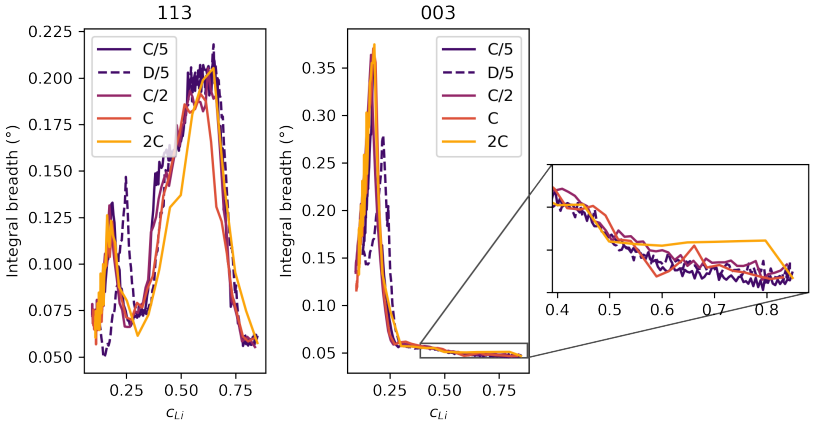

Figure S23: Integral breadth (IB) of 113 and 003 Bragg reflections of LNO as function of lithium content c_{Li} for increasing charge rates (C/5, C/2, C, 2C).

18 Characterisation of common derivatives features

The derivatives $\mathrm{d}V/\mathrm{d}c_{Li}$ and $\mathrm{d}V/\mathrm{d}q$ as a function of c_{Li} are plotted for NMC622, NMC811 and LNO in Figure S24. Once again, the derivatives features does not depend on the C-rate when plotted as a function of c_{Li} for the three materials. These curves could be used by battery manufacturers to limit the accessible c_{Li} range of the layered TM oxides active materials. The critical lithium content 0.4 can be detected in NMC811 and LNO as the third bump of $\mathrm{d}V/\mathrm{d}q$, if the bump at $c_{Li} \simeq 0.8$ is the bump number one. More straightforward in NMC811 and LNO, $c_{Li} = 0.4$, is then detected as the third zero of $\mathrm{d}^2V/\mathrm{d}q^2$. The detection of the critical value in NMC622 is more complex since the $\mathrm{d}V/\mathrm{d}q$ has no obvious specific feature near that region.

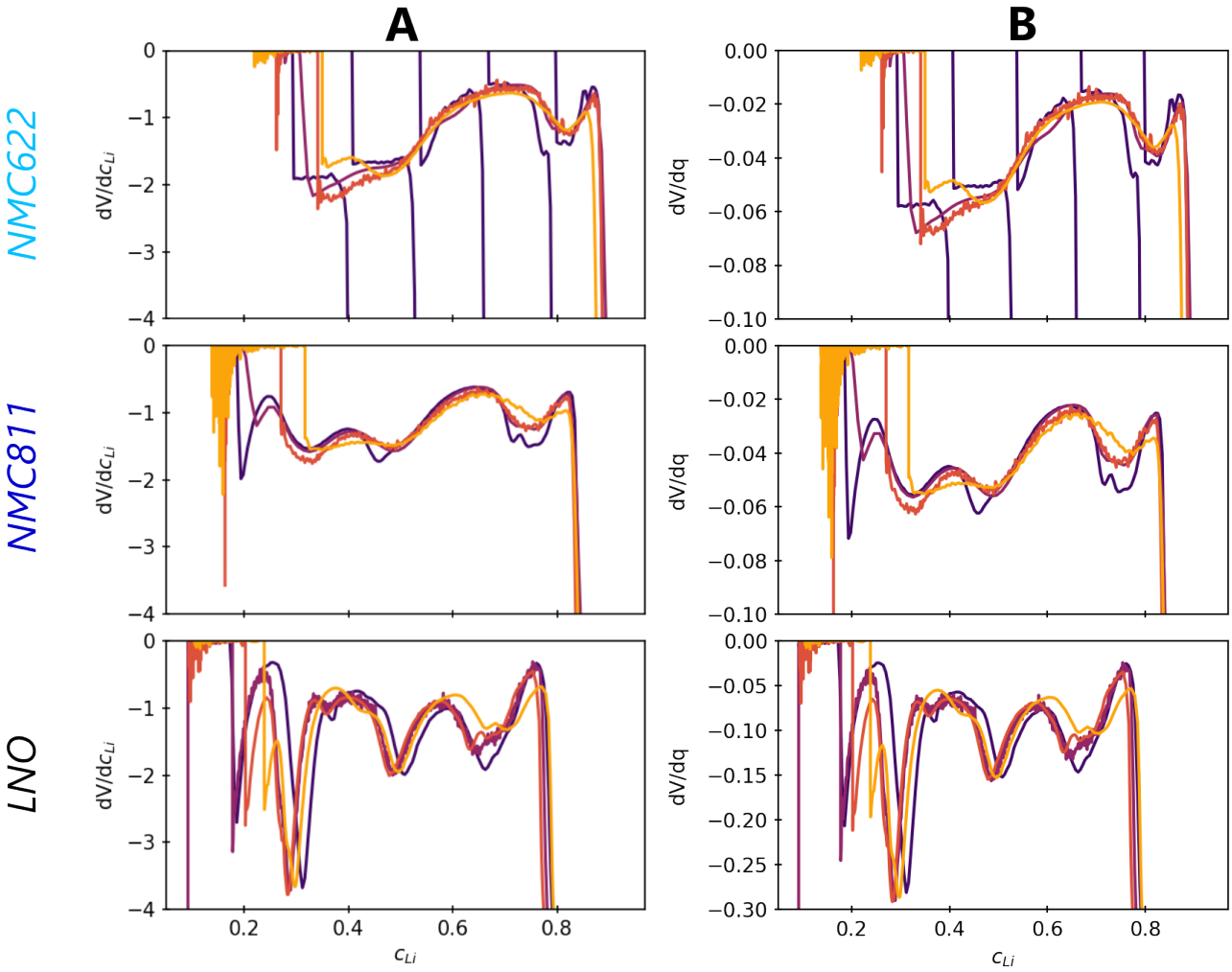

Figure S24: Derivatives of (A) $\mathrm{d}V/\mathrm{d}c_{Li}$ and (B) $\mathrm{d}V/\mathrm{d}q$ as a function of c_{Li} for NMC622, NMC811 and LNO from top to bottom, respectively.

References

[1] M. Hekmatfar, I. Hasa, R. Eghbal, D. V. Carvalho, A. Moretti, and S. Passerini, "Effect of electrolyte additives on the lini0.5mn0.3co0.2o2 surface film formation with lithium and graphite negative electrodes," *Adv. Mater. Interfaces*, vol. 7, no. 1, p. 1901500, 2020.

[2] Y. Qian, P. Niehoff, M. Börner, M. Grützke, X. Mönnighoff, P. Behrends, S. Nowak, M. Winter, and F. M. Schappacher, "Influence of electrolyte additives on the cathode electrolyte interphase (cei) formation on lini1/3mn1/3co1/3o2 in half cells with li metal counter electrode," *J Power Sources*, vol. 329, pp. 31–40, 2016.

[3] V. Soleimanian and S. R. Aghdaee, "Comparison methods of variance and line profile analysis for the evaluation of microstructures of materials," *Powder Diffr*, vol. 23, no. 1, p. 41–51, 2008.

[4] K. Märker, P. J. Reeves, C. Xu, K. J. Griffith, and C. P. Grey, "Evolution of structure and lithium dynamics in $LiNi_{0.8}Mn_{0.1}Co_{0.1}O_2$ (NMC811) cathodes during electrochemical cycling," *Chem. Mater.*, vol. 31, no. 7, pp. 2545–2554, 2019.

[5] A. Grenier, P. J. Reeves, H. Liu, I. D. Seymour, K. Märker, K. M. Wiaderek, P. J. Chupas, C. P. Grey, and K. W. Chapman, "Intrinsic kinetic limitations in substitued lithium-layered transition-metal oxide electrodes," *J. Am. Chem. Soc.*, vol. 142, no. 15, pp. 7001–7011, 2020.

[6] V. Charbonneau, A. Lasia, and G. Brisard, "Impedance studies of Li+ diffusion in nickel manganese cobalt oxide (NMC) during charge/discharge cycles," *J. Electroanal. Chem.*, vol. 875, p. 113944, 2020. Special Issue in Memory of Andrzej Wieckowski.

[7] S.-L. Wu, W. Zhang, X. Song, A. K. Shukla, G. Liu, V. Battaglia, and V. Srinivasan, "High rate capability of li(ni1/3mn1/3co1/3)o2 electrode for li-ion batteries," *J Electrochem Soc*, vol. 159, p. A438, jan 2012.

[8] G. Qian, Y. Zhang, L. Li, R. Zhang, J. Xu, Z. Cheng, S. Xie, H. Wang, Q. Rao, Y. He, Y. Shen, L. Chen, M. Tang, and Z.-F. Ma, "Single-crystal nickel-rich layered-oxide battery cathode materials: synthesis, electrochemistry, and intra-granular fracture," *Energy Storage Mater*, vol. 27, pp. 140–149, 2020.